THE JOURNAL OF PHYSICAL CHEMISTRY A

Article

pubs.acs.org/JPCA

# Probing the Heterogeneous Ozonolysis of Squalene Nanoparticles by Photoemission

Michael I. Jacobs,[†,‡] Bo Xu,[‡] Oleg Kostko,[‡] Nadja Heine,[‡] Musahid Ahmed,[‡] and Kevin R. Wilson*[,‡]

[†]Department of Chemistry, University of California, Berkeley, California 94720, United States

[‡]Chemical Sciences Division, Lawrence Berkeley National Laboratory, Berkeley, California 94720, United States

**ABSTRACT:** The heterogeneous reaction of ozone ($O_3$) with 200 nm squalene nanoparticles is studied using near-edge X-ray absorption fine structure (NEXAFS) and ultraviolet (UPS) and X-ray photoelectron spectroscopy (XPS). Photoelectrons are detected from free nanoparticle beams using a velocity map imaging (VMI) spectrometer capable of detecting photoelectrons with up to 40 eV of kinetic energy. Heterogeneous kinetics are quantified using changes in the UPS, XPS, and NEXAFS spectrum, yielding uptake coefficients for the decay of the double bonds in squalene of $(3.1 \pm 0.7) \times 10^{-4}$, $(2.6 \pm 0.6) \times 10^{-4}$, and $(2.9 \pm 0.7) \times 10^{-4}$, respectively. When comparing these values with the uptake coefficient, $(1.0 \pm 0.2) \times 10^{-3}$, determined by the molecular decay of squalene measured with aerosol mass spectrometry, it is found that on average 1.6 ± 0.2 double bonds are removed for each ozone-squalene reactive collision, suggesting the importance of evaporation of small molecular weight reaction products from the aerosol. From further analysis of the nanoparticle XPS spectrum, it is found that ozonolysis increases the oxygen-to-carbon (O:C) ratio of the aerosol to 0.43 ± 0.03 and produces 16 ± 4% and 84 ± 4% secondary ozonides and carbonyls, respectively. The methods developed here show how aerosol photoemission can be used to quantify heterogeneous reaction on free nanoparticles.

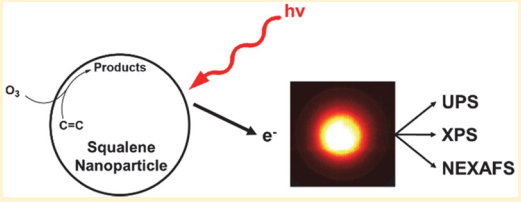


## I. INTRODUCTION

Aerosol surfaces play a significant role in heterogeneous chemical reactions in the atmosphere with larger scale impacts on both human health[1] and climate.[2] Recent investigations suggest that secondary organic aerosol (SOA), particles derived from the condensation of nonvolatile organic gas phase species, can exist in a semisolid, diffusion-limited state.[3,4] Evaporation[5−7] and heterogeneous oxidation[8−11] studies suggest that diffusion limitations lead to the formation of interfacial chemical gradients within aerosol particles. Since heterogeneous chemistry is largely controlled by the species present at the surface, these steep chemical gradients are expected to change the atmospheric fate of aerosol by altering mechanisms for water uptake, condensation of gas phase species, and oxidation.

So far the study of the chemistry on diffusion-limited aerosol has been accomplished by aerosol methods, which probe the chemistry of the entire particle volume, such as aerosol mass spectrometry (AMS),[12] scanning transmission X-ray microscopy,[13] scanning electron microscopy,[14] etc., or methods that probe loss of gas phase species due to uptake onto surfaces.[9,15] These techniques are not able to directly measure the chemical species at the surface, nor the formation and dissipation of chemical gradients within the particle. Thus, alternative methods (such as photoelectron spectroscopy) are needed to study the surfaces of particles undergoing atmospheric reactions.

Photoelectron spectroscopy is surface sensitive due to the short inelastic mean free path of photoelectrons.[16] Several experiments have used ultraviolet photoelectron spectroscopy (UPS) to study the electronic structure of free nanoparticles.[17−22] Additionally, X-ray photoelectron spectroscopy (XPS) studies have probed free nanoparticles to provide elemental information on the surface.[23−26] Due to instrumental constraints, XPS has been primarily used to study heterogeneous chemistry on thin films or monolayers.[27−30] Similarly, near-edge X-ray absorption fine structure (NEXAFS) measurements have been performed on both free[31,32] and deposited nanoparticles.[13,33,34] However, studying aerosol chemistry with NEXAFS has been limited to probing deposited particles.[15] Deposition may alter the physical and chemical properties of aerosol, motivating the need to study free particles. In this work, we use a velocity map imaging (VMI) spectrometer that is capable of detecting photoelectrons with up to 40 eV of kinetic energy to probe the chemistry of free aerosol particles using VUV and X-ray photoelectron spectroscopy. This instrument is used to measure heterogeneous uptake coefficients and to determine how the surface composition of squalene aerosol changes upon oxidation by $O_3$.

Squalene ($C_{30}H_{50}$) is a branched, unsaturated (six double bonds) hydrocarbon. The six double bonds in squalene react readily with ozone ($O_3$).[35] As the single most abundant component found on human skin (accounting for ∼10% of surface lipids),[36] squalene is the most significant ozone reactive constituent in indoor environments.[37] Because of its reactivity and relative importance for indoor air quality, several studies

**Received:** September 7, 2016
**Revised:** October 11, 2016
**Published:** October 17, 2016





DOI: 10.1021/acs.jpca.6b09061
J. Phys. Chem. A XXXX, XXX, XXX−XXX

have measured the kinetics and products of squalene ozonolysis using either attenuated total reflection infrared spectroscopy (ATR-IR)[38,39] or mass spectrometry.[37,40,41] While capable of measuring reaction kinetics and (for the case of mass spectrometry) products, it is difficult to obtain quantitative product yields with either of these techniques; mass spectrometry suffers from differences in ionization efficiencies, and IR intensity convolutes both concentration and orientation. Because photoelectron intensity scales directly with the number of species present, it is capable of quantitatively measuring product formation via functional group yields.

In the present study, we examine the heterogeneous ozonolysis of squalene nanoparticles using UPS, XPS, and NEXAFS techniques. We combine these photoemission approaches with the molecular information obtained via aerosol mass spectrometry to construct a self-consistent picture of the heterogeneous reaction rate and product yields observed during the reaction. Ultimately, the methods developed here will directly be applied to studying the surface chemistry of semisolid, diffusion-limited aerosol particles.

## II. EXPERIMENTAL METHODS

**II.a. Flow Tube Setup.** The heterogeneous ozonolysis of squalene is performed using a flow tube reactor. Details of the experimental setup have been described elsewhere,[42,43] but a short description and schematic (Figure 1) are presented here.

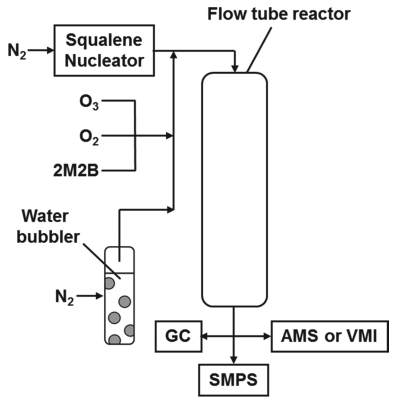


**Figure 1.** Schematic of flow tube setup (2M2B = 2-methyl-2-butene, GC = gas chromatograph, SMPS = scanning mobility particle sizer, AMS = VUV aerosol mass spectrometer, VMI = velocity map imaging spectrometer).

Squalene nanoparticles are formed via homogeneous nucleation by passing dry $N_2$ over a heated reservoir (135 °C for AMS experiments and 150 °C for VMI experiments) containing pure squalene. As the flow cools, particles nucleate into sizes that are log-normal in distribution with an average particle size of ∼200 ± 40 nm. The particle laden flow is mixed with ozone, humidified and dry $N_2$, and $O_2$. 2-Methyl-2-butene (2M2B) is added to the flow as a gas phase ozone tracer. The total flow rate is kept at 1 L/min, with 0−6 ppm ozone, 30% relative humidity (RH), 10% oxygen, and 0.5 ppm 2M2B. Particles react in an atmospheric pressure flow tube reactor (140 cm length, 2.5 cm i.d.) with an average residence time of ∼37 s.

The decay of the gas phase tracer is monitored with a gas chromatograph (GC) equipped with a flame ionization detector (SRI Instruments). Changes to the particle size distribution are monitored with a scanning mobility particle sizer (SMPS, TSI). After oxidation, the aerosol is sampled into either a vacuum ultraviolet aerosol mass spectrometer (VUV-AMS)[44] to determine particle composition or a VMI spectrometer to measure particle photoemission.

**II.b. VUV-AMS Measurements.** The chemical composition of the aerosol is determined using a home-built tunable vacuum ultraviolet photoionization aerosol mass spectrometer (VUV-AMS), previously described.[44] Briefly, a collimated particle beam is generated using an aerodynamic lens. The particles are vaporized as they impinge on a heated copper block (140 °C). Vaporized aerosol components are ionized using VUV radiation and detected in a time-of-flight mass spectrometer. A photon energy of 9.6 eV is used in the majority of experiments, which were conducted at the Chemical Dynamics Beamline (9.0.2) at the Advanced Light Source (ALS), Lawrence Berkeley National Laboratory (LBNL).

**II.c. X-ray (XPS) and Ultraviolet (UPS) Photoelectron Spectroscopy.** Aerosol photoemission is detected using a home-built velocity map imaging (VMI) spectrometer. A schematic of the spectrometer is shown in Figure 2a. Aerosol

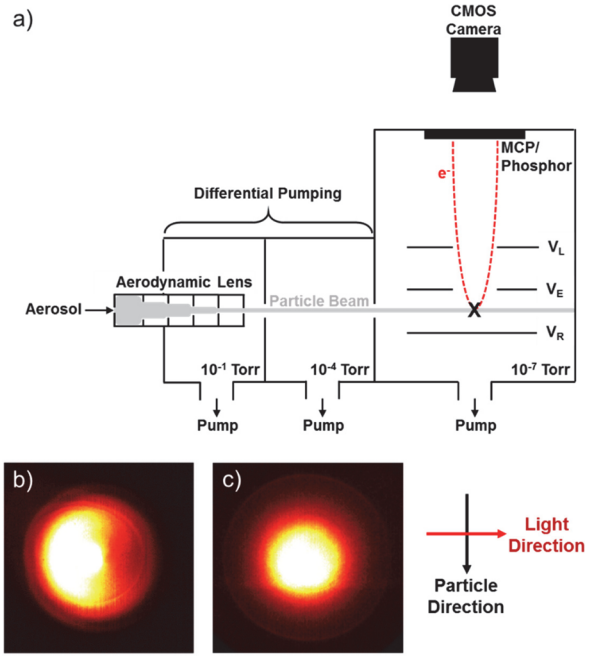


**Figure 2.** (a) Schematic of the VMI spectrometer. (b) UPS image of squalene nanoparticles collected at $E$ = 15 eV. (c) XPS image of squalene nanoparticles collected at $E$ = 310 eV.

particles pass through a 150 $\mu$m flow limiting orifice (with a flow rate of 2.5 $cm^3/s$) into an aerodynamic lens. The aerodynamic lens consists of five separate apertures that focus the particles into a tightly collimated beam.[45] A similar aerodynamic lens configuration has been used extensively in our lab in both previous VMI and VUV-AMS measurements.[17,18,44] The beam of particles passes through two stages of differential pumping into the interaction region where the particle and photon beams intersect at 90°. The operating pressure in the interaction region is $\sim 10^{-7}$ Torr. Residual water vapor and gas phase organic species in the interaction region are removed by a liquid nitrogen trap.

The VMI spectrometer consists of three electrodes: repeller, extractor, and lens. Photoelectrons are produced as the particle beam intersects synchrotron radiation between the repeller and extractor electrodes. Voltages are applied to the electrodes to


DOI: 10.1021/acs.jpca.6b09061
J. Phys. Chem. A XXXX, XXX, XXX−XXX

achieve "velocity mapping" conditions where all electrons with the same momentum in the plane of the detector are imaged to the same point.[46] Electrons are accelerated toward a dual multichannel plate coupled to a fast phosphor screen (both made by Photonis). The images are collected using a CMOS camera. The 2-D photoelectron images represent a projection of the nascent 3-D photoelectron velocity distribution. Using typical image processing techniques (BASEX[47] and pBASEX[48]), the 3-D velocity distribution can be reconstructed. By integrating angularly, a speed distribution can be extracted and then converted to a kinetic energy distribution.

The image collection procedure for the UPS and XPS experiments is similar. Image accumulation times are 300−500 s. At each oxidation condition, images are collected in triplicate. A background image is collected by placing a HEPA particle filter in line with the flow limiting orifice. The background image is subtracted from the data image to obtain a final image with signal arising from only particles. UPS measurements and all X-ray measurements were conducted at the ALS at the Chemical Dynamics Beamline 9.0.2 and Beamline 6.0.2, respectively.

An example squalene UPS image is shown in Figure 2b. The asymmetry in the image is due to the shallow penetration depth of the VUV radiation.[18−20,49] From the refractive index of squalene, 15 eV light only penetrates ∼6.5 nm into the nanoparticle.[50] Thus, photoemission is significantly preferred from the "front side" of the particle (where light impinges on the particle and photon flux is largest) leading to the angular asymmetry observed in Figure 2b (i.e., shadowing of the particle).[19,49]

Figure 2c shows an example of a squalene XPS image. Compared to the UPS image, the XPS image is more symmetric. Soft X-rays are expected to penetrate several microns in squalene (compared to ∼6.5 nm for VUV radiation), which means incident X-rays will ionize molecules uniformly throughout the particle, and thus, unlike the VUV case, there is no preference in the direction of electron emission. Despite the long penetration lengths of X-rays, it is the short inelastic mean free path of emitted C 1s photoelectrons that makes the technique surface sensitive.

The study of free nanoparticles with XPS is in its infancy, with only a few publications. Most of the previous studies use an aerodynamic lens coupled with a hemispherical electron analyzer, which requires long collection times.[23−25] A conventional hemispherical energy analyzer has an acceptance angle of up to ∼44°[51] compared with the $4\pi$ collection efficiency of VMI spectrometers, which allows for an order of magnitude improvement in collection efficiency. Based on typical aerosol concentrations (∼$2 \times 10^6$ particles/cm$^3$ as measured by the SMPS) and a flow rate of 2.5 cm$^3$/s through the aerodynamic lens, particles are introduced to the VMI spectrometer at a rate of $5 \times 10^6$ particles/s. Under ideal conditions, the particle beam is focused to ∼100 $\mu$m with particles traveling roughly 150 m/s.[12] The estimated size of the incident X-ray beam from beamline 6.0.2 is ∼200 × 200 $\mu$m. Based on the size of the interaction region and the speed of the particles, we estimate there are 6−7 particles in the X-ray interaction region at any one time. If the particles have a diameter of 200 nm and the entire cross section is available for probing, then we estimate that particles only account for ∼$(5 \times 10^{-4})$% of the interaction region. The estimated flux at 310 eV is $3 \times 10^{11}$ photons/s. Thus, based on the flux and cross-sectional area of the particles in the interaction region, only ∼$2 \times 10^6$ photons/s (or ∼0.4 photons/particle) strike the particles. This indicates that multiple ionization events are unlikely and charging effects minimal.

**II.d. Near Edge X-ray Extended Fine Structure (NEXAFS) Measurements.** NEXAFS spectroscopy involves the excitation of core level electrons into unoccupied bound or continuum states. Because the partially filled and empty states are often diffuse and influenced by surrounding molecules, NEXAFS is a sensitive probe of the bonding environment around a molecule. Additionally, by looking for specific spectroscopic transitions (such as the 1s → $\pi^*$ double bond feature), NEXAFS can be used as a probe of functional groups.[52]

Partial electron yield (PEY) NEXAFS measurements of free aerosol particles are collected by measuring the intensity of secondary electrons. Shown in Figure 3a is a typical photoelectron kinetic energy distribution from squalene nanoparticles probed with 310 eV X-rays. The high signal intensity at low kinetic energies is due to secondary electrons. Secondary electrons result from the inelastic scattering of higher energy electrons (such as photoelectrons or Auger electrons).[53] Thus, the intensity of the secondary electrons is directly related to the absorption cross section of the particle.

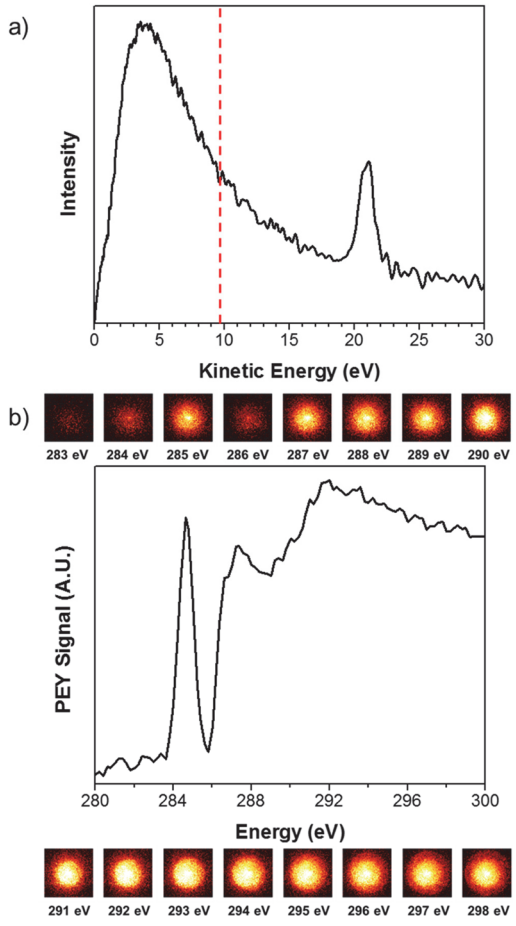


**Figure 3.** (a) Example squalene XPS measurement at 310 eV photon energy. The low kinetic energy secondary electrons (<10 eV, left of red line) are used to measure NEXAFS spectra. (b) Squalene carbon K edge NEXAFS spectrum derived from low kinetic energy secondary electrons. Selected images of squalene photoemission to demonstrate differences in secondary electron intensity are shown.



DOI: 10.1021/acs.jpca.6b09061
J. Phys. Chem. A XXXX, XXX, XXX−XXX

Carbon and oxygen K edge NEXAFS measurements are collected by scanning the beamline photon energy from 280 to 300 eV and 528−556 eV, respectively. The energy step-size for both carbon and oxygen K edge NEXAFS spectra is 0.2 eV. At each energy, images are collected for 10 s. A PEY NEXAFS spectrum is obtained by summing over the center of a background-subtracted image (e.g., photoelectrons with KE < 10 eV as shown in Figure 3a). A photodiode located at the back of the VMI spectrometer is used to measure photon flux vs energy, which is needed to normalize the electron signals. An example carbon K edge NEXAFS spectrum of squalene aerosol with selected images is shown in Figure 3b.

The NEXAFS spectra are normalized before kinetics are extracted. The carbon K edge NEXAFS spectra are area normalized using the PEY signal from 286 to 300 eV (the signal after the 1s → $\pi^*$ transition). The oxygen K edge NEXAFS spectra are normalized to the pre-edge intensity (528−529 eV). This background signal in the oxygen K edge NEXAFS spectra is proportional to the surface area of the particles (as measured with the SMPS) and results from carbon K edge absorption at lower energies.

**II.e. Kinetic Analysis.** For each measurement, an effective uptake coefficient ($\gamma_{eff}$) is quantified. $\gamma_{eff}$ is the number of molecules consumed per $O_3$ collision with the particle. The magnitude of $\gamma_{eff}$ may depend upon the experimental technique employed. For example, $\gamma_{eff}$ can be computed from either the molecular decay of squalene (i.e., mass spectrometry) or by the decay of its C=C functional groups (i.e., UPS, NEXAFS, and XPS). In a "closed" system, where chemical species cannot leave the particle, the molecule-derived uptake coefficient ($\gamma_{M,eff}$) and functional group-derived uptake coefficient ($\gamma_{FG,eff}$) are related simply by

$$\gamma_{M,eff} = FG \cdot \gamma_{FG,eff} \quad (1)$$

where FG is the number of functional groups. Deviation from this relationship occurs when functional groups leave the particle (such as reaction products with double bonds evaporating from the particle). If there is no evaporation from the particle, the ratio of $\gamma_{M,eff}$ to $\gamma_{FG,eff}$ would be 6 (the number of double bonds in squalene). If ozonolysis products with double bonds can evaporate from the particle, then $\gamma_{FG,eff}$ would appear larger because there are more apparent double bonds removed from the particle per $O_3$ collision. In this case, $\gamma_{M,eff}$ (which is independent of how products react) would remain constant, and the ratio of $\gamma_{M,eff}$ to $\gamma_{FG,eff}$ would be less than 6. Thus, the ratio of $\gamma_{M,eff}$ to $\gamma_{FG,eff}$ provides a quantitative metric of evaporation of double bonds from the particle.

To compute $\gamma_{eff}$, a bimolecular heterogeneous ozonolysis rate constant is determined. First, the average ozone exposure in the reactor is quantified using the GC to monitor the decay of the gas phase tracer, 2M2B. Ozone exposure is equal to

$$\frac{\ln([2M2B]/[2M2B]_0)}{k_{2M2B}} = \int [O_3]dt = \langle O_3 \rangle_t \cdot t \quad (2)$$

where $[2M2B]_0$ and [2M2B] are the concentration of 2M2B before and after oxidation, $k_{2M2B}$ is the gas phase ozonolysis rate constant of 2M2B ($(4.1 \pm 0.5) \times 10^{-16}$ cm$^3$ molecule$^{-1}$ s$^{-1}$),[54] and $\langle O_3 \rangle_t \cdot t$ is the ozone exposure. Rate constants are determined from either the decay or growth of a spectral feature with increased ozone exposure. If a measurement is sensitive to the decay of squalene or its double bonds (e.g., VUV-AMS, $\pi$-bond peak in UPS, double bonded carbon peak ($C_{C=C}$) in XPS, 1s → $\pi^*$ in carbon K-edge NEXAFS), the normalized decay at a given ozone exposure is fit to

$$\ln \frac{[signal]}{[signal]_0} = -k_{eff} \langle O_3 \rangle_t \cdot t \quad (3)$$

where [signal] and $[signal]_0$ are the final and initial signal levels, $k_{eff}$ is the effective heterogeneous rate constant, and $\langle O_3 \rangle_t \cdot t$ is the ozone exposure as measured by the decay of 2M2B. When a measurement is sensitive to the growth of oxidized features (e.g., O/C ratio in XPS and oxygen K edge in NEXAFS), the data are fit to the following function:

$$[signal] = [signal]_{max}(1 - e^{-k_{eff}\langle O_3 \rangle \cdot t}) \quad (4)$$

where $[signal]_{max}$ is the value that the data asymptotically approach (i.e., at high ozone exposures). The rate constant is then used to compute an effective uptake coefficient:[42]

$$\gamma_{eff} = \frac{2k_{eff}D_{surf}\rho_0 N_A}{3\bar{c}M} \quad (5)$$

where $D_{surf}$ is the measured mean surface weighted particle diameter, $\rho_0$ is the density, $N_A$ is Avogadro's number, $\bar{c}$ is the mean speed of gas-phase ozone, and $M$ is the molecular weight. This formulation of $\gamma_{eff}$ uses the bimolecular heterogeneous rate constant and calculated flux of ozone molecules on the particles surface to determine the reaction probability. Because $\gamma_{eff}$ does not separate secondary reactions that occur within the particle from the primary oxidative event, it is possible to have $\gamma_{eff}$ that are greater than one.[55−58]

## III. RESULTS AND DISCUSSION

This section is organized as follows: We first describe the oxidation products and kinetics measured by the VUV-AMS, which will be used to inform and constrain the fitting and analysis of the XPS data presented in section III.d. In sections III.b and III.c, UPS and NEXAFS data are presented and analyzed, respectively. Finally, we summarize the experimental results in the context of previous measurements.

**III.a. Oxidation Products and Kinetics via VUV-AMS.** The VUV-AMS is used to determine the products and molecule-specific kinetics of squalene ozonolysis. Shown in Figure 4a is an aerosol mass spectrum of squalene obtained before reaction with ozone. The effective uptake coefficient is calculated by plotting the normalized decay of the squalene ion signal ($m/z$ = 410 in Figure 4a) vs ozone exposure. The effective uptake coefficient for squalene ozonolysis determined here, $(1.0 \pm 0.2) \times 10^{-3}$, is slightly larger than previous measurements of squalene ozonolysis, which range from $1 \times 10^{-5}$ to $4.5 \times 10^{-4}$.[38−41] The uptake coefficient reported by Wells et al. ($4.5 \times 10^{-4}$)[40] is derived from the loss of ozone (as opposed to the loss of squalene) and thus is not sensitive to potential secondary reactions that might occur in the particle. However, the uptake coefficients reported by Petrick and Dubowski[39] and Fu et al.[38] ($1 \times 10^{-5}$ and $1.7 \times 10^{-4}$, respectively) are obtained from ATR-IR measurements, which are sensitive to the decay of a double bond spectral feature. Assuming minimal evaporative loss (which will be discussed later), these uptake coefficients can be scaled by the number of double bonds in the parent molecule (six for squalene) to convert them from functional group specific to molecule specific uptake coefficients (eq 1). With this correction, our reported uptake coefficient is consistent with that reported by Fu et al. (both nominally $1 \times 10^{-3}$). Petrick and Dubowski


DOI: 10.1021/acs.jpca.6b09061
J. Phys. Chem. A XXXX, XXX, XXX−XXX

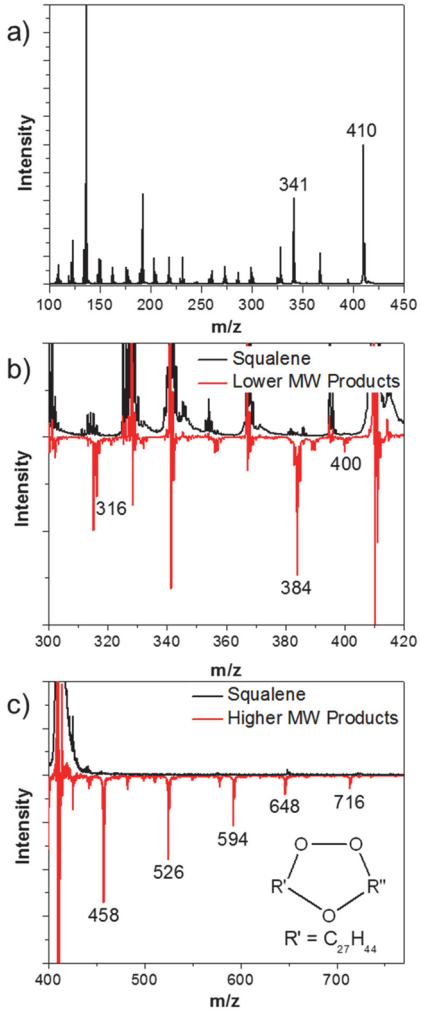


**Figure 4.** (a) Squalene mass spectrum. The molecular squalene ion ($m/z$ 410) and a fragment ($m/z$ 341) are labeled. (b) Difference mass spectrum (red) of lower molecular weight ozonolysis products. Oxidized squalene is subtracted from nonoxidized squalene (black). The ions at $m/z$ 316 and 384 correspond to carbonyl containing products. The ion at $m/z$ 400 is an acid containing product. (c) Difference mass spectrum (red) of higher molecular weight ozonolysis products. Oxidized squalene is subtracted from nonoxidized squalene (black). Molecular formulas for R″ in the products with $m/z$ 458, 526, 594, 648, and 716 are $C_3H_6$, $C_8H_{14}$, $C_{13}H_{22}$, $C_{17}H_{28}$, and $C_{22}H_{36}$, respectively. The ozone exposure is ~2.5 × $10^{14}$ molecule s $cm^{-3}$ for both product spectra.

attribute the low uptake coefficient they report to a thicker squalene layer where not all molecules are available for reaction, in contrast to squalene monolayers in other work.[39] The uptake coefficient reported recently by Zhou et al.[41] ($4.3 \times 10^{-4}$ Table 1) is determined by probing a thin squalene film (i.e., monolayer) with mass spectrometry to monitor the decay of squalene. The discrepancy between the molecular uptake coefficient reported here ($1.0 \times 10^{-3}$) and that of Zhou et al. cannot be currently explained, although we note that the ozone concentrations used by Zhou et al. are significantly lower than those used here and perhaps contribute to this difference. For example, there could be differences in the amount of secondary chemistry at high ozone concentrations that result in the higher apparent uptake coefficient observed here.

The reaction pathways of a generic alkene with ozone are summarized in Scheme 1.[59] Briefly, ozone is expected to react with the double bond creating a primary ozonide. This primary ozonide will decompose into a carbonyl and a Criegee intermediate (CI). Depending on surrounding reactants, the CI can react in a variety of different ways. It can rearrange unimolecularly to form a carbonyl (R1) or an acid (R2), or it can react with a carbonyl compound to yield a secondary ozonide (R3). Additionally, two CIs can react to form a peroxide compound (R4), which can decompose into two carbonyl compounds at room temperature.[60] At higher RH, the CI can also react with water to create a hydroxyhydroperoxide (R5), which is thought to be in equilibrium with a carbonyl compound and hydrogen peroxide.[61] Oligomers can form when multiple Criegee intermediates react with one molecule.

Shown in Figure 4b,c are reaction products detected using mass spectrometry. Difference spectra (shown in red in Figure 4b,c) clearly show the formation of both lower molecular weight and higher molecular weight ozonolysis products. Lower molecular weight, carbonyl-containing products are observed at $m/z$ 316 and 384. These ions are consistent with products containing four and five double bonds, respectively. Additionally, a small peak is detected at $m/z$ 400 corresponding to an acid product with five double bonds. The ratio of the peak at $m/z$ 384 to $m/z$ 400 is ~10:1, which (assuming equal photoionization cross sections) suggests that the acid formation channel, under our experimental conditions, is negligible. This is consistent with previous measurements of the ozonolysis of oleic acid, which observed significantly more carbonyl than acid products.[62] Dissociative photoionization of squalene and its higher molecular weight products makes it difficult to assign products with molecular weights less than $m/z$ 200.

In addition to the lower molecular weight products, ions at $m/z$ 458, 526, 594, 648, and 716 are consistent with the formation of higher molecular weight secondary ozonides. These products result from a CI with five double bonds reacting with a carbonyl containing zero to four double bonds. The secondary ozonides are in good agreement with other ozonolysis studies that have detected higher molecular weight, oligomeric products.[60,63,64] It is clear from the mass spectra that there are two major classes of reaction products, secondary ozonides and carbonyls, which will be used to constrain the analysis of the photoemission data presented below.

**III.b. UPS Spectra and Kinetics.** UPS spectra of pure nanoparticles from squalene and two other unsaturated molecules, oleic acid ($C_{18}H_{34}O_2$, one double bond) and linoleic acid ($C_{18}H_{32}O_2$, two double bonds), are presented in Figure 5a. The photon energy for each spectrum is 15 eV. All three of these spectra show a similar low binding energy ($E_b \approx$ 8 eV) feature whose intensity scales with the number of double bonds. Furthermore, this low binding energy feature decreases when squalene reacts with ozone (Figure 5b). The spectral comparisons between the different unsaturated acids and oxidized squalene nanoparticles as well as previous measurements of squalene's optical properties[50,65] suggest that $\pi$-bonding electrons are responsible for the feature at $E_b$ = 8 eV. By quantifying the decay of this $\pi$-bond peak, the UPS spectra can serve as a functional group specific probe of ozonolysis.

For simplicity, the UPS spectra are fit by two Gaussian functions: one corresponding to a $\pi$-bond peak (binding energy of 8.0 eV) and a feature representing the conglomerate of $\sigma$-bonds (with a binding energy centered around 11.5 eV).[50] As squalene is oxidized, the same two Gaussian functions are fit to each spectra. Fitting the decay of the $\pi$-bond peak to eq 3 (Figure 5c) yields a double bond-specific, effective uptake


DOI: 10.1021/acs.jpca.6b09061
J. Phys. Chem. A XXXX, XXX, XXX−XXX

**Table 1. Summary of Effective Uptake Coefficients and Their Comparison to the Molecule Specific Uptake Coefficient for the Various Spectroscopic Probes[a]**

| | effective uptake coefficient | ratio of molecular $\gamma_{eff}$ to C=C FG $\gamma_{eff}$ | double bonds lost per reaction |
|---|---|---|---|
| **Molecule Specific Probe** | | | |
| mass spectrometry (molecular ion) | $(1.0 \pm 0.2) \times 10^{-3}$ | | |
| Zhou et al.[41] | $(4.3 \pm 2.2) \times 10^{-4}$ | | |
| Wells et al.[40] | $(4.5 \pm 1.4) \times 10^{-4}$ | | |
| Petrick and Dubowski[39] | $1 \times 10^{-5}$ | | |
| **Double Bond Probe** | | | |
| UPS (pi-bond peak) | $(3.1 \pm 0.7) \times 10^{-4}$ | $3.2 \pm 1.0$ | $1.9 \pm 0.6$ |
| C K-edge NEXAFS (1s → $\pi^*$) | $(2.6 \pm 0.6) \times 10^{-4}$ | $3.8 \pm 1.2$ | $1.6 \pm 0.5$ |
| XPS ($C_{C=C}$ peak) | $(2.9 \pm 0.7) \times 10^{-4}$ | $3.4 \pm 1.1$ | $1.8 \pm 0.6$ |
| Fu et al.[38] | $(1.7 \pm 0.17) \times 10^{-4}$ | | |
| **Functionalization Probe** | | | |
| O K-edge NEXAFS (PEY intensity) | $(2.6 \pm 0.6) \times 10^{-4}$ | $3.8 \pm 1.2$ | $1.6 \pm 0.5$ |
| XPS (C=O and C−O peaks) | $(2.4 \pm 0.7) \times 10^{-4}$ | $4.2 \pm 1.5$ | $1.4 \pm 0.5$ |

[a]Squalene ozonolysis uptake coefficients from previous measurements are included for comparison.

**Scheme 1. Simplified Alkene Ozonolysis Mechanism and Expected Products[a]**

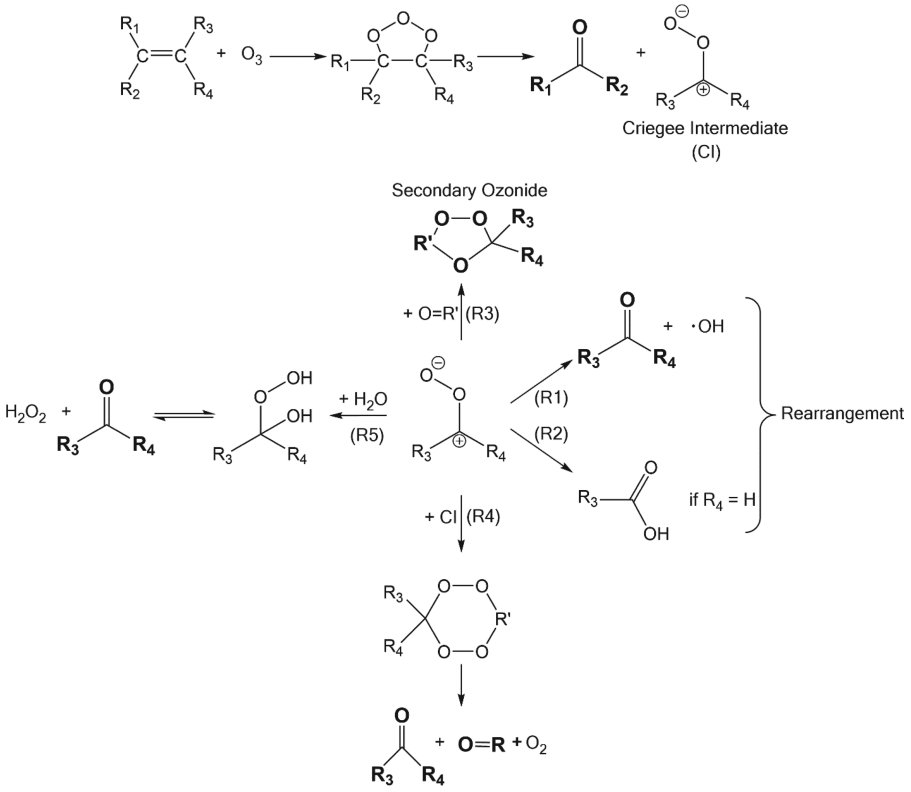


[a]Bolded species are observed in the VUV-AMS spectra and included in XPS data fitting.

coefficient of $(3.1 \pm 0.7) \times 10^{-4}$. This uptake coefficient in the context of the other measured uptake coefficients will be discussed below.

**III.c. NEXAFS Spectra and Kinetics.** Both carbon and oxygen K edge NEXAFS spectra are collected as a function of ozone exposure. The carbon K edge NEXAFS spectra are shown in Figure 6a. The pure squalene spectrum shows an intense feature at ~284.6 eV. This feature has been assigned to the 1s → $\pi^*$ transition.[52] When squalene reacts and the double bonds are cleaved, the intensity of this transition decreases. As shown in Figure 6b, the decay of this 1s → $\pi^*$ feature with ozone follows an exponential function, whose rate coefficient from eq 3 is used to obtain a double bond-specific effective uptake coefficient of $(2.6 \pm 0.6) \times 10^{-4}$.

Previously, in a study monitoring the reaction of ozone with shikimic acid particles, the decay of the 1s → $\pi^*$ transition was used to extract an effective uptake coefficient.[15] Additionally, Moffet et al. have looked at the NEXAFS spectra of individual deposited aerosol and inferred compositional information from distinct spectroscopic transitions.[34] While a full analysis of our spectra is not possible due to the limited collected energy range, our NEXAFS spectra lack a prominent carboxylic acid feature (a peak at 288.4 eV).[34] This is consistent with the VUV-AMS results and supports the conclusion that carboxylic acid product formation is negligible.


DOI: 10.1021/acs.jpca.6b09061
J. Phys. Chem. A XXXX, XXX, XXX−XXX

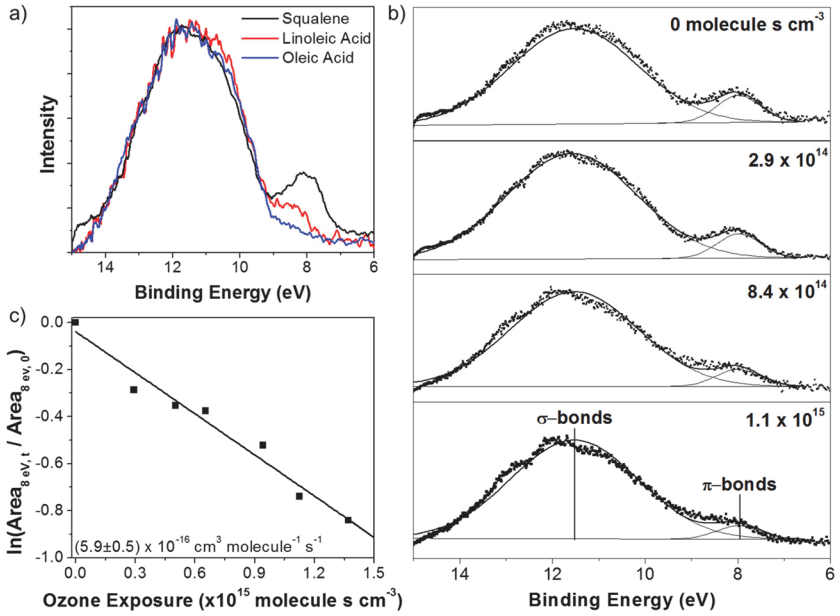


**Figure 5.** (a) UPS spectra of nanoparticles with differing numbers of double bonds. Squalene, linoleic acid, and oleic acid each have six, two, and one double bonds, respectively. As the number of double bonds increases, the low binding energy feature increases. (b) UPS spectra at various oxidation conditions. The two peaks present are conglomeration of $\sigma$-bonds peak (11.4 eV) and $\pi$-bond peak (8 eV). (c) Kinetics of squalene $\pi$-bond peak decay. The heterogeneous rate ozonolysis rate constant is on the lower left.

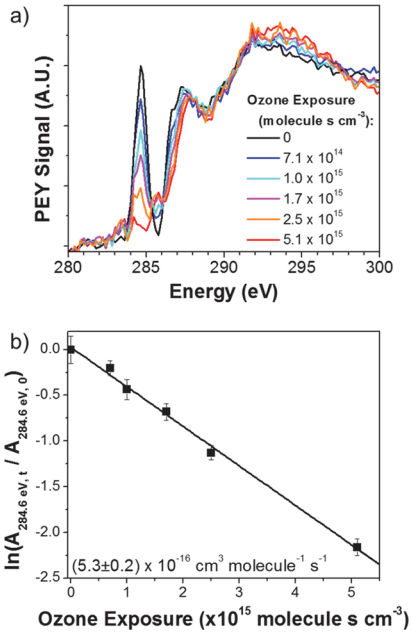


**Figure 6.** (a) Squalene carbon K edge NEXAFS spectra at various ozone exposures. (b) Kinetics of the 1s $\rightarrow$ $\pi^*$ transition decay (284.6 eV).

A direct measure of the oxygen added to the particle is achieved from analysis of oxygen K edge NEXAFS spectra. As expected and shown in Figure 7a, pure squalene does not exhibit any spectra intensity at the oxygen K edge. As the particle is oxidized and the oxygen content within the particle increases, there is an increase in the oxygen K edge intensity. In Figure 7b, the rise in intensity of the oxygen peak at 532.2 eV is fit to eq 4 to yield a product-derived effective uptake coefficient of $(2.6 \pm 0.6) \times 10^{-4}$. The agreement of the carbon and oxygen K edge uptake coefficients will be discussed below.

Oxygen K edge NEXAFS spectra of pure diester (bis-(ethylhexyl) sebacate, BES) nanoparticles are collected in order to help explain the features observed in the NEXAFS spectra of oxidized squalene. Figure 7c shows a comparison of oxidized squalene and pure BES. As can be seen in the NEXAFS spectrum of BES, there are two peaks: one arising from the carbonyl 1s $\rightarrow$ $\pi^*$ transition (531.6 eV) and one arising from the O−C ester bond (534.4 eV).[52] Compared to the BES spectrum, the transition in the oxidized squalene spectrum is broader and encompasses the 1s $\rightarrow$ $\pi^*$ and O−C ester transitions observed in BES. The change in the width can be attributed to the number of species present; more species with slightly different chemical structures will absorb at slightly different energies. The shift in the energy of the transitions suggests that both carbonyl 1s $\rightarrow$ $\pi^*$ and O−C transitions are present in the oxidized squalene particle. The shapes of the squalene oxygen K edge NEXAFS spectra are constant throughout oxidation, and only the intensity of the oxygen absorption changes. This suggests that the squalene ozonolysis reaction mechanism and oxygenated products formed do not change as a result of the species present.

**III.d. XPS Measurements.** C 1s XPS spectra of squalene at different oxidation conditions are collected at a photon energy of 310 eV and are presented in Figure 8a. The spectra show that as squalene reacts with ozone, a peak at ~292.3 eV emerges. Additionally, the peak at ~289 eV shifts to higher energy and broadens. The apparent shift to higher binding energy is attributed to the loss of double bond carbons. The broadening of the 289 eV peak and the emergence of the 292.3 eV peak are consistent with the formation of new oxygenated reaction products, which the VUV-AMS measurements suggest are primarily carbonyls and secondary ozonides.

To extract quantitative functional group information as a function of ozone exposure, the C 1s spectra are fit using a method adapted from a previous study.[27] Because resolution is expected to be instrument limited and not determined by lifetime broadening, all of the peaks are fit to Gaussian


DOI: 10.1021/acs.jpca.6b09061
J. Phys. Chem. A XXXX, XXX, XXX−XXX

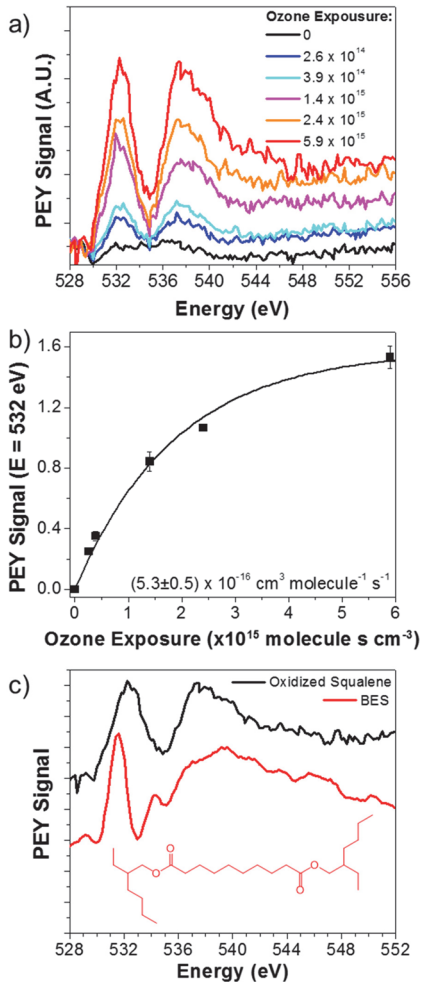


**Figure 7.** (a) Squalene oxygen K edge NEXAFS spectra at various ozone exposures. (b) Kinetics of the emergence of the peak at 532 eV. (c) Comparison of oxidized squalene and bis(ethylhexyl) sebacate (BES) oxygen K edge NEXAFS spectra.

functions. The peak positions and widths (full width at half-maximum, fwhm) for double bonded carbon ($C_{C=C}$) and methylene carbon ($CH_x$) are determined first. The position of the $CH_x$ peak is determined using the most highly oxidized squalene spectrum (containing a negligible amount of $C_{C=C}$). Then the unreacted pure squalene spectrum is used to determine the position of the $C_{C=C}$ peak and the FWHMs of both $CH_x$ and $C_{C=C}$. A couple of additional constraints are imposed during the analysis: (i) the FWHMs of $CH_x$ and $C_{C=C}$ are assumed to be equal; and (ii) the ratio of $CH_x$ to $C_{C=C}$ peak areas in the unoxidized squalene spectrum is constrained to the stoichiometric ratio of $CH_x$ to $C_{C=C}$ in the squalene molecule (i.e., 18 $CH_x$/12 $C_{C=C}$). This results in $C_{C=C}$ and $CH_x$ peaks that are separated by 0.6 eV with FWHMs of 1.2 eV.

The oxygenated carbon species are then fit in the remaining XPS spectra based on the following assumptions: (i) The FWHMs of all carbon species are equal (1.2 eV); (ii) Based on the VUV-AMS product data, COOH functional groups are not observed to be significant and are therefore not included in the XPS fit; (iii) Only two types of carbon containing reaction products, consistent with the VUV-AMS results, are present, carbon from carbonyl compounds (C═O) and carbon from secondary ozonides (C−O); (iv) The ozonolysis reactions (and evaporation of products from the particle) do not significantly change the total fraction of $CH_x$ in the particle. This last assumption is made after examining the expected products of ozonolysis and tabulating the different types of carbon present. The fraction of $CH_x$ to total carbon does not vary more than ±2%. Because the particles are well-mixed and the surface composition is assumed to mimic the bulk composition, the area of $CH_x$ in each spectrum is constrained to be 60% of the total carbon area. The positions of the C═O and C−O peaks are determined from the most oxidized squalene spectrum. The C═O and C−O shifts relative to the $CH_x$ peak are 2.9 and 1.3 eV, respectively. The four peaks are fit to the remaining spectra at different ozone exposures (Figure 8a). The fraction of each carbon species present at different ozone exposures is determined from calculated peak areas (Figure 8b).

In summary, the photoelectron spectra are fit with four total components. The C 1s peak assignments (shown in Figure 8a) have chemical shifts (relative to the $CH_x$ feature) of 0.6 eV for $C_{C=C}$, 1.3 eV for C−O, and 2.9 eV for C═O. The fitting procedure yields chemical shifts for $C_{C=C}$ and C═O that are consistent with literature values.[27,66] The secondary ozonides (shown in Figure 4c) have a carbon bound to two oxygens: an ether and a peroxide linkage. To the best of our knowledge a reference XPS spectrum for such a functional has not been reported. Based on other reference spectra, the chemical shift of carbon increases roughly with its oxidation state. The oxidation state of the carbon in the secondary ozonide is between that of an ether and a carbonyl. Thus, the chemical shift is expected to be between an ether and carbonyl (~1.4−3.0 eV).[66] The C−O peak that we attribute to the secondary ozonide is shifted by 1.3 eV. While this is on the low end of expected chemical shift, the secondary ozonide is the only product that is consistent with the ozonolysis mechanism and the VUV-AMS data that accounts for this spectral feature.

Heterogeneous reaction kinetics are determined using the change in $C_{C=C}$, C═O, and C−O peak areas. The decay of the $C_{C=C}$ peak provides another double bond specific probe. In Figure 8b, the normalized decay of the $C_{C=C}$ peak is fit to eq 3 to yield a double bond-derived $\gamma_{eff}$ of $(2.9 \pm 0.6) \times 10^{-4}$. The change in the O/C ratio of the particle can be quantified using the C═O and C−O peaks. If each C−O peak is part of a secondary ozonide, each C−O carbon contributes 1.5 oxygen atoms. Thus, the O/C ratio can be estimated as

$$\mathrm{O/C} = F(\mathrm{C{=}O}) + \frac{3}{2}F(\mathrm{C{-}O}) \quad (6)$$

where $F$(C═O) and $F$(C−O) are the fractional peak area of C═O and C−O, respectively. Figure 8c shows the O/C ratio as a function of ozone exposure. Comparing the C−O and C═O peak areas at each ozone exposure shows that secondary ozonides (oligomeric products) and carbonyls (fragmentation products) account for 16 ± 4% and 84 ± 4% of the oxygenated carbon, respectively. This ratio does not change with oxidation and can be used to calculate a maximum O/C ratio (to constrain the growth kinetics). Replacing every double bonded carbon with 16 ± 4% secondary ozonide and 84 ± 4% carbonyl results in a maximum O/C ratio of 0.43 ± 0.03. These data are fit to eq 4 (with $[\mathrm{signal}]_{max}$ constrained to 0.43) yielding a product-specific effective uptake coefficient of $(2.4 \pm 0.7) \times 10^{-4}$. The observation of secondary ozonides in both the VUV-AMS and C 1s XPS data suggests that (on average) more than one oxygen atom is added to each carbon in a double bond. Double bonded carbons account for 40% of the total carbon in the original squalene molecule. Thus, a final O/C greater than


DOI: 10.1021/acs.jpca.6b09061
J. Phys. Chem. A XXXX, XXX, XXX−XXX

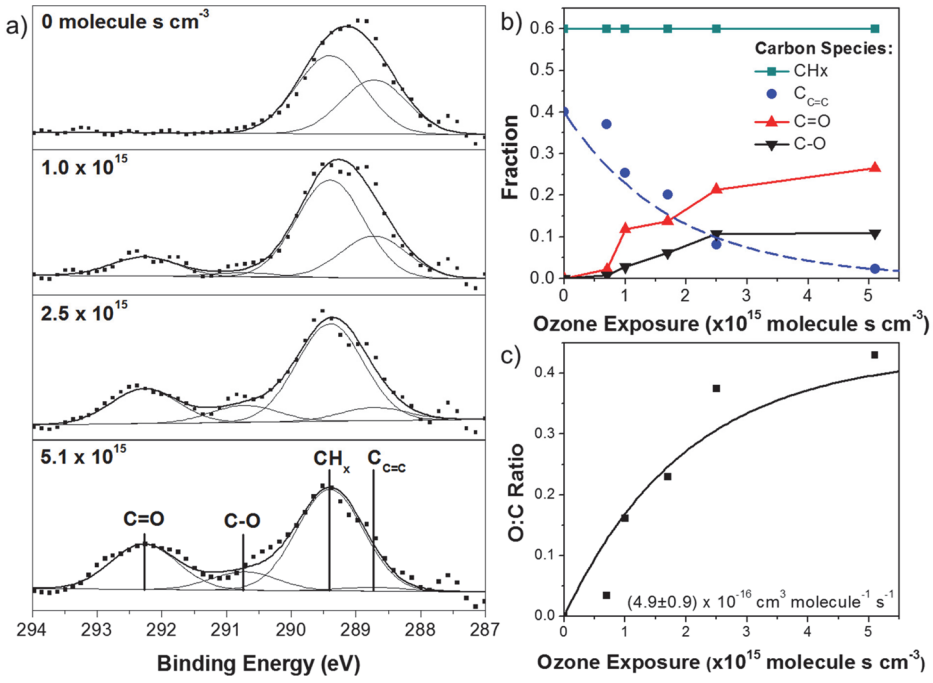


**Figure 8.** (a) XPS spectra of squalene at various oxidation conditions showing the results of the final fitting procedure. The four peaks present (from left to right) are C═O, C−O, $CH_x$, and $C_{C=C}$. (b) Fractional peak area of the four types of carbon present. Kinetics of the $C_{C=C}$ decay are included (blue dashed line, $k = (5.9 \pm 0.5) \times 10^{-16}$ cm$^3$ molecule$^{-1}$ s$^{-1}$). (c) Kinetics of the change in the O/C ratio as the particle is oxidized.

0.4 is consistent with the products observed with the VUV-AMS.

Most studies have used mass spectrometry to measure secondary ozonides and oligomeric products of ozonolysis,[60,62−64,67] where accurate quantification is difficult without calibration standards. Observed in this work, the secondary ozonide (oligomeric) and carbonyl (fragmentation) yields measured here, 16 ± 4% and 84 ± 4%, respectively, have not been previously reported for squalene ozonolysis. However, measurements of ozonide product yields from oleic acid have been reported. The yield of secondary ozonides (and diperoxides) from oleic acid ozonolysis ranges from ∼10%[64] to 68%.[60] The discrepancy between previous measurements could be attributed to differences in quantification or reaction conditions. For example, a change in the relative humidity can affect the yield of ozonolysis products because water reacts with the CI.[59,68] The CI is expected to readily react with the acid functional group found in oleic acid to create higher molecular weight species.[60] Because the formation of acids is not observed as a dominant product channel for squalene ozonolysis, a direct comparison of ozonide yields from oleic acid and squalene ozonolysis is not straightforward. Even so, our 16 ± 4% ozonide yield at a 30% RH is fairly consistent with what has been measured previously. These higher molecular weight peroxide species are thought to be potential skin irritants,[69] making an accurate measure of their yield desirable.

Because the CI can react in several different bimolecular pathways, the measured product yields are expected to be dependent upon reaction conditions. Changing the reaction conditions can alter the chemical species that are present, affecting product formation rates. For example, at lower relative humidity the rate of hydroxyhydroperoxide formation (R5) is expected to decrease, and the importance of unimolecular reactions (R1 and R2) will increase. This is consistent with results reported by Zhou et al., who recently observed enhanced acid formation at low RH.[41] Additionally, at higher ozone exposures more CI and carbonyl product species will be present, which will enhance their reactions with a newly formed CI (R3 and R4). Thus, the product yields reported here are not expected to be the same at significantly different reaction conditions.

**III.e. Summary of Measurements.** A summary of the effective uptake coefficients is presented in Table 1. The double bond effective uptake coefficients and functionalization uptake coefficients agree within experimental error. Compared to the double bond-derived $\gamma_{eff}$ from Fu et al. ($1.7 \times 10^{-4}$),[38] the effective uptake coefficients measured by the photoemission probes are slightly larger. A comparison of molecular $\gamma_{eff}$ (i.e., VUV-AMS results) and C═C functional group $\gamma_{eff}$ (i.e., UPS, XPS, and NEXAFS results) provides insight into how double bonds are removed from the particle. As discussed above, if the particle represents a closed system where no chemical species evaporate, then the ratio of the molecular $\gamma_{eff}$ to the C═C functional group $\gamma_{eff}$ should be 6 (the number of double bonds in squalene). However, as shown in Table 1, the measured ratios fall between 3 and 4. Evaporation of lower molecular weight products from the particle would account for this discrepancy. Volatile products that contain a double bond can evaporate from the particle, and thus, multiple double bonds can be removed from the particle with only one ozonolysis reaction. Previous studies that monitored the gas phase products of squalene ozonolysis detected carbonyl species containing one to three double bonds in the gas phase.[37,40] Comparing the measured ratio of molecular $\gamma_{eff}$ to C═C functional group $\gamma_{eff}$ to the expected ratio of a closed system can provide insight into how many double bonds are removed from the particle for every ozonolysis reaction. We estimate that for each ozonolysis reaction, there are roughly 1.6 ± 0.2 double bonds removed from the particle (Table 1). Thus, evaporation of reaction products leads to additional depletion of double


DOI: 10.1021/acs.jpca.6b09061
J. Phys. Chem. A XXXX, XXX, XXX−XXX

bonds from the particle and a further decrease in aerosol reactivity with $O_3$. While earlier studies have detected evaporative products from squalene ozonolysis,[37,40] the extent to which evaporation and ozonolysis each contribute to the loss of functional groups from the particle has not been previously measured.

## IV. CONCLUSION

We have measured the kinetics of the ozonolysis of squalene nanoparticles using a suite of photoemission techniques: UPS, carbon and oxygen K edge NEXAFS, and C 1s XPS. These photoemission probes provide direct measurements of double bonds as well as oxidized products that are formed. Coupled with molecule specific VUV-AMS measurements, the kinetics measured by the photoemission probes suggest that for each ozonolysis reaction roughly 1.6 ± 0.2 double bonds are removed from the particle. Unsaturated lipids on human skin (such as squalene) serve as a first line of dermal defense against oxidizing agents in the air.[37] The evaporative loss of products with double bonds suggests that squalene's role in preventing oxidative damage to human skin is slightly mitigated as not all of its double bonds will remain surface bound for oxidation. C 1s XPS measurements also provide a direct quantification of secondary ozonide yield, 16 ± 4%. This direct measurement marks an improvement on previous measurements, which rely on estimates of ionization efficiencies for mass spectrometry.

Overall, the methods developed studying the ozonolysis of squalene could be applied to more complicated, unknown surfaces. We believe that this work will serve to inform the study of surfaces in diffusion-limited systems where chemical gradients are expected to form as a result of atmospheric aging.

## AUTHOR INFORMATION

### Corresponding Author

*E-mail: krwilson@lbl.gov. Tel: (510) 495-2474.

### Notes

The authors declare no competing financial interest.

## ACKNOWLEDGMENTS

This work and the Advanced Light Source were supported by the Director, Office of Energy Research, Office of Basic Energy Science of the U.S. Department of Energy under Contract No. DE-AC02-05CH11231. M.I.J. thanks the NSF for an NSF Graduate Research Fellowship under DGE-1106400. K.R.W. was supported by the Department of Energy, Office of Science Early Career Research Program. We thank Lena Trotochaud, Osman Karslioglu, and Hendrik Bluhm for discussions about XPS fitting. We also thank Royce Lam for discussions about NEXAFS data interpretations.

## REFERENCES

(1) Pope, A. C., III; Dockery, D. W. Health Effects of Fine Particulate Air Pollution: Lines that Connect. *J. Air Waste Manage. Assoc.* **2006**, *56*, 709−742.

(2) Boucher, O.; Randall, D.; Artaxo, P.; Bretherton, C.; Feingold, G.; Forster, P.; Kerminen, V.-M.; Kondo, Y.; Liao, H.; Lohmann, U.; et al. Clouds and Aerosols. In *Climate Change 2013: The Physical Science Basis: Contribution of Working Group I to the Fifth Assessment Report of the Intergovernmental Panel on Climate Change*; Cambridge University Press: Cambridge, UK, 2013; pp 571−657.

(3) Virtanen, A.; Joutsensaari, J.; Koop, T.; Kannosto, J.; Yli-Pirilä, P.; Leskinen, J.; Mäkelä, J. M.; Holopainen, J. K.; Pöschl, U.; Kulmala, M.; et al. An amorphous solid state of biogenic secondary organic aerosol particles. *Nature* **2010**, *467* (7317), 824−827.

(4) Koop, T.; Bookhold, J.; Shiraiwa, M.; Pöschl, U. Glass transition and phase state of organic compounds: dependency on molecular properties and implications for secondary organic aerosols in the atmosphere. *Phys. Chem. Chem. Phys.* **2011**, *13* (43), 19238−19255.

(5) Cappa, C. D.; Wilson, K. R. Evolution of organic aerosol mass spectra upon heating: Implications for OA phase and partitioning behavior. *Atmos. Chem. Phys.* **2011**, *11* (5), 1895−1911.

(6) Abramson, E.; Imre, D.; Beránek, J.; Wilson, J.; Zelenyuk, A. Experimental determination of chemical diffusion within secondary organic aerosol particles. *Phys. Chem. Chem. Phys.* **2013**, *15* (8), 2983−2991.

(7) Vaden, T. D.; Imre, D.; Beránek, J.; Shrivastava, M.; Zelenyuk, A. Evaporation kinetics and phase of laboratory and ambient secondary organic aerosol. *Proc. Natl. Acad. Sci. U. S. A.* **2011**, *108* (6), 2190−2195.

(8) Kuwata, M.; Martin, S. T. Phase of atmospheric secondary organic material affects its reactivity. *Proc. Natl. Acad. Sci. U. S. A.* **2012**, *109* (43), 17354−17359.

(9) Shiraiwa, M.; Ammann, M.; Koop, T.; Pöschl, U. Gas uptake and chemical aging of semisolid organic aerosol particles. *Proc. Natl. Acad. Sci. U. S. A.* **2011**, *108* (27), 11003−11008.

(10) Zhou, S.; Shiraiwa, M.; McWhinney, R. D.; Pöschl, U.; Abbatt, J. P. D. Kinetic limitations in gas-particle reactions arising from slow diffusion in secondary organic aerosol. *Faraday Discuss.* **2013**, *165*, 391−406.

(11) Berkemeier, T.; Steimer, S. S.; Krieger, U. K.; Peter, T.; Pöschl, U.; Ammann, M.; Shiraiwa, M. Ozone uptake on glassy, semi-solid and liquid organic matter and the role of reactive oxygen intermediates in atmospheric aerosol chemistry. *Phys. Chem. Chem. Phys.* **2016**, *18* (18), 12662−12674.

(12) Jayne, J. T.; Leard, D. C.; Zhang, X.; Davidovits, P.; Smith, K. a.; Kolb, C. E.; Worsnop, D. R. Development of an Aerosol Mass Spectrometer for Size and Composition Analysis of Submicron Particles. *Aerosol Sci. Technol.* **2000**, *33* (1−2), 49−70.

(13) Maria, S. F.; Russell, L. M.; Gilles, M. K.; Myneni, S. C. B. Organic Aerosol Growth Mechanisms and Their Climate-Forcing Implications. *Science (Washington, DC, U. S.)* **2004**, *306* (5703), 1921−1924.

(14) Laskin, A.; Iedema, M. J.; Cowin, J. P. Time-Resolved Aerosol Collector for CCSEM/EDX Single-Particle Analysis. *Aerosol Sci. Technol.* **2003**, *37* (3), 246−260.

(15) Steimer, S. S.; Lampimaki, M.; Coz, E.; Grzinic, G.; Ammann, M. The influence of physical state on shikimic acid ozonolysis: A case for in situ microspectroscopy. *Atmos. Chem. Phys.* **2014**, *14* (19), 10761−10772.

(16) Tanuma, S.; Powell, C. J.; Penn, D. R. Calculations of Electron Inelastic Mean Free Paths. *Surf. Interface Anal.* **1994**, *21*, 165−176.

(17) Wilson, K. R.; Peterka, D. S.; Jimenez-Cruz, M.; Leone, S. R.; Ahmed, M. VUV photoelectron imaging of biological nanoparticles: ionization energy determination of nanophase glycine and phenyl-alanine-glycine-glycine. *Phys. Chem. Chem. Phys.* **2006**, *8* (16), 1884−1890.

(18) Wilson, K.; Zou, S.; Shu, J.; Rühl, E. Size-dependent angular distributions of low-energy photoelectrons emitted from NaCl nanoparticles. *Nano Lett.* **2007**, *7* (7), 2014−2019.

(19) Berg, M. J.; Wilson, K. R.; Sorensen, C. M.; Chakrabarti, A.; Ahmed, M. Discrete dipole approximation for low-energy photo-electron emission from NaCl nanoparticles. *J. Quant. Spectrosc. Radiat. Transfer* **2012**, *113* (3), 259−265.

(20) Goldmann, M.; Miguel-Sánchez, J.; West, A. H. C.; Yoder, B. L.; Signorell, R. Electron mean free path from angle-dependent photoelectron spectroscopy of aerosol particles. *J. Chem. Phys.* **2015**, *142* (22), 224304.

(21) West, A. H. C.; Yoder, B. L.; Signorell, R. Size-dependent velocity map photoelectron imaging of nanosized ammonia aerosol particles. *J. Phys. Chem. A* **2013**, *117* (50), 13326−13335.



DOI: 10.1021/acs.jpca.6b09061
J. Phys. Chem. A XXXX, XXX, XXX−XXX

(22) Shu, J.; Wilson, K. R.; Ahmed, M.; Leone, S. R. Coupling a versatile aerosol apparatus to a synchrotron: Vacuum ultraviolet light scattering, photoelectron imaging, and fragment free mass spectrometry. *Rev. Sci. Instrum.* **2006**, *77* (4), 0−10.
(23) Mysak, E. R.; Starr, D. E.; Wilson, K. R.; Bluhm, H. Note: A combined aerodynamic lens/ambient pressure x-ray photoelectron spectroscopy experiment for the on-stream investigation of aerosol surfaces. *Rev. Sci. Instrum.* **2010**, *81* (1), 16106.
(24) Antonsson, E.; Patanen, M.; Nicolas, C.; Neville, J. J.; Benkoula, S.; Goel, A.; Miron, C. Complete Bromide Surface Segregation in Mixed NaCl/NaBr Aerosols Grown from Droplets. *Phys. Rev. X* **2015**, *5*, 11025.
(25) Sublemontier, O.; Nicolas, C.; Aureau, D.; Patanen, M.; Kintz, H.; Liu, X.; Gaveau, M.; Garrec, J. Le; Robert, E.; Barreda, F. X-ray Photoelectron Spectroscopy of Isolated Nanoparticles. *J. Phys. Chem. Lett.* **2014**, *5*, 3399−3403.
(26) Meinen, J.; Khasminskaya, S.; Eritt, M.; Leisner, T.; Antonsson, E.; Langer, B.; Rühl, E. Core level photoionization on free sub-10-nm nanoparticles using synchrotron radiation. *Rev. Sci. Instrum.* **2010**, *81* (8), 085107.
(27) Mysak, E. R.; Smith, J. D.; Ashby, P. D.; Newberg, J. T.; Wilson, K. R.; Bluhm, H. Competitive reaction pathways for functionalization and volatilization in the heterogeneous oxidation of coronene thin films by hydroxyl radicals and ozone. *Phys. Chem. Chem. Phys.* **2011**, *13* (16), 7554−7564.
(28) Moise, T.; Rudich, Y. Uptake of Cl and Br by organic surfaces - A perspective on organic aerosols processing by tropospheric oxidants. *Geophys. Res. Lett.* **2001**, *28* (21), 4083−4086.
(29) Knopf, D. A.; Mak, J.; Gross, S.; Bertram, A. K. Does atmospheric processing of saturated hydrocarbon surfaces by NO 3 lead to volatilization? *Geophys. Res. Lett.* **2006**, *33* (17), 1−5.
(30) Molina, M. J.; Ivanov, a. V.; Trakhtenberg, S.; Molina, L. T. Atmospheric evolution of organic aerosol. *Geophys. Res. Lett.* **2004**, *31* (22), L22104.
(31) Antonsson, E.; Bresch, H.; Lewinski, R.; Wassermann, B.; Leisner, T.; Graf, C.; Langer, B.; Ruhl, E. Free nanoparticles studied by soft X-rays. *Chem. Phys. Lett.* **2013**, *559*, 1−11.
(32) Lewinski, R.; Graf, C.; Langer, B.; Flesch, R.; Bresch, H.; Wassermann, B.; Ruhl, E. Size-effects in clusters and free nanoparticles probed by soft X-rays. *Eur. Phys. J.: Spec. Top.* **2009**, *169* (1), 67−72.
(33) Takahashi, Y.; Kanai, Y.; Kamioka, H.; Ohta, A.; Maruyama, H.; Song, Z.; Shimizu, H. Speciation of Sulfate in Size-Fractionated Aerosol Particles Using Sulfur K-edge X-ray Absorption Near-Edge Structure. *Environ. Sci. Technol.* **2006**, *40* (16), 5052−5057.
(34) Moffet, R. C.; Henn, T.; Laskin, A.; Gilles, M. K. Automated chemical analysis of internally mixed aerosol particles using X-ray spectromicroscopy at the carbon K-edge. *Anal. Chem.* **2010**, *82* (19), 7906−7914.
(35) Criegee, R. Mechanism of Ozonolysis. *Angew. Chem., Int. Ed. Engl.* **1975**, *14* (11), 745−752.
(36) Weschler, C. J. Roles of the human occupant in indoor chemistry. *Indoor Air* **2016**, *26* (1), 6−24.
(37) Wisthaler, A.; Weschler, C. J. Reactions of ozone with human skin lipids: sources of carbonyls, dicarbonyls, and hydroxycarbonyls in indoor air. *Proc. Natl. Acad. Sci. U. S. A.* **2010**, *107* (15), 6568−6575.
(38) Fu, D.; Leng, C.; Kelley, J.; Zeng, G.; Zhang, Y.; Liu, Y. ATR-IR study of ozone initiated heterogeneous oxidation of squalene in an indoor environment. *Environ. Sci. Technol.* **2013**, *47* (18), 10611−10618.
(39) Petrick, L.; Dubowski, Y. Heterogeneous oxidation of squalene film by ozone under various indoor conditions. *Indoor Air* **2009**, *19* (5), 381−391.
(40) Wells, J. R.; Spicer, C.; Morrison, G. C.; Dean, S. W.; Coleman, B. K. Kinetics and Reaction Products of Ozone and Surface-Bound Squalene. *J. ASTM Int.* **2008**, *5* (JULY), 101629.
(41) Zhou, S.; Forbes, M. W.; Abbatt, J. P. D. Kinetics and Products from Heterogeneous Oxidation of Squalene with Ozone. *Environ. Sci. Technol.* **2016**, DOI: 10.1021/acs.est.6b03270.
(42) Smith, J. D.; Kroll, J. H.; Cappa, C. D.; Che, D. L.; Liu, C. L.; Ahmed, M.; Leone, S. R.; Worsnop, D. R.; Wilson, K. R. The heterogeneous reaction of hydroxyl radicals with sub-micron squalane particles: A model system for understanding the oxidative aging of ambient aerosols. *Atmos. Chem. Phys.* **2009**, *9* (9), 3209−3222.
(43) Kroll, J. H.; Smith, J. D.; Che, D. L.; Kessler, S. H.; Worsnop, D. R.; Wilson, K. R. Physical chemistry of aerosols. *Phys. Chem. Chem. Phys.* **2009**, *11* (36), 7759.
(44) Gloaguen, E.; Mysak, E. R.; Leone, S. R.; Ahmed, M.; Wilson, K. R. Investigating the chemical composition of mixed organic-inorganic particles by "soft" vacuum ultraviolet photoionization: The reaction of ozone with anthracene on sodium chloride particles. *Int. J. Mass Spectrom.* **2006**, *258* (1−3), 74−85.
(45) Liu, P.; Ziemann, P. J.; Kittelson, D. B.; McMurry, P. H. Generating Particle Beams of Controlled Dimensions and Divergence: II. Experimental Evaluation of Particle Motion in Aerodynamic Lenses and Nozzle Expansions. *Aerosol Sci. Technol.* **1995**, *22* (3), 314−324.
(46) Eppink, A. T. J. B.; Parker, D. H. Velocity map imaging of ions and electrons using electrostatic lenses: Application in photoelectron and photofragment ion imaging of molecular oxygen Velocity map imaging of ions and electrons using electrostatic lenses: Application in photoelectron and. *Rev. Sci. Instrum.* **1997**, *68*, 3477−3484.
(47) Dribinski, V.; Ossadtchi, A.; Mandelshtam, V. a.; Reisler, H. Reconstruction of Abel-transformable images: The Gaussian basis-set expansion Abel transform method. *Rev. Sci. Instrum.* **2002**, *73* (7), 2634.
(48) Garcia, G. A.; Nahon, L.; Powis, I. Two-dimensional charged particle image inversion using a polar basis function expansion. *Rev. Sci. Instrum.* **2004**, *75* (11), 4989−4996.
(49) Signorell, R.; Goldmann, M.; Yoder, B. L.; Bodi, A.; Chasovskikh, E.; Lang, L.; Luckhaus, D. Nanofocusing, shadowing, and electron mean free path in the photoemission from aerosol droplets. *Chem. Phys. Lett.* **2016**, *658*, 1.
(50) Painter, L. R.; Attrey, J. S.; Hubbell, H. H.; Birkhoff, R. D. Vacuum ultraviolet optical properties of squalane and squalene. *J. Appl. Phys.* **1984**, *55* (3), 756.
(51) Specs Gmbh, Berlin, Germany.
(52) Stohr, J. *NEXAFS Spectroscopy*; Springer: Berlin, 1996.
(53) Hufner, S. *Photoelectron Spectroscopy: Priciples and Applications*, 3rd ed.; Springer, 2003.
(54) Witter, M.; Berndt, T.; Böge, O.; Stratmann, F.; Heintzenberg, J. Gas-phase ozonolysis: Rate coefficients for a series of terpenes and rate coefficients and OH yields for 2-methyl 2-butene and 2,3-dimethyl-2-butene. *Int. J. Chem. Kinet.* **2002**, *34* (6), 394−403.
(55) Nah, T.; Kessler, S. H.; Daumit, K. E.; Kroll, J. H.; Leone, S. R.; Wilson, K. R. OH-initiated oxidation of sub-micron unsaturated fatty acid particles. *Phys. Chem. Chem. Phys.* **2013**, *15* (42), 18649−18663.
(56) Nah, T.; Kessler, S. H.; Daumit, K. E.; Kroll, J. H.; Leone, S. R.; Wilson, K. R. Influence of molecular structure and chemical functionality on the heterogeneous OH-initiated oxidation of unsaturated organic particles. *J. Phys. Chem. A* **2014**, *118* (23), 4106−4119.
(57) Richards-Henderson, N. K.; Goldstein, A. H.; Wilson, K. R. Large Enhancement in the Heterogeneous Oxidation Rate of Organic Aerosols by Hydroxyl Radicals in the Presence of Nitric Oxide. *J. Phys. Chem. Lett.* **2015**, *6*, 4451−4455.
(58) Richards-Henderson, N. K.; Goldstein, A. H.; Wilson, K. R. Sulfur Dioxide Accelerates the Heterogeneous Oxidation Rate of Organic Aerosol by Hydroxyl Radicals. *Environ. Sci. Technol.* **2016**, *50* (7), 3554−3561.
(59) Bailey, P. S. *Ozonation in Organic Chemistry*, Vol. *1*.; Academic Press: New York, 1978.
(60) Ziemann, P. J. Aerosol products, mechanisms, and kinetics of heterogeneous reactions of ozone with oleic acid in pure and mixed particles. *Faraday Discuss.* **2005**, *130*, 469−490.
(61) Zhao, R.; Lee, A. K. Y.; Soong, R.; Simpson, A. J.; Abbatt, J. P. D. Formation of aqueous-phase α-hydroxyhydroperoxides (α-HHP): Potential atmospheric impacts. *Atmos. Chem. Phys.* **2013**, *13* (12), 5857−5872.


DOI: 10.1021/acs.jpca.6b09061
J. Phys. Chem. A XXXX, XXX, XXX−XXX

(62) Zahardis, J.; Petrucci, G. A. The oleic acid-ozone heterogeneous reaction system: products, kinetics, secondary chemistry, and atmospheric implications of a model system − a review. *Atmos. Chem. Phys.* **2007**, *7*, 1237−1274.
(63) Fooshee, D. R.; Aiona, P. K.; Laskin, A.; Laskin, J.; Nizkorodov, S. a.; Baldi, P. F. Atmospheric Oxidation of Squalene: Molecular Study Using COBRA Modeling and High-Resolution Mass Spectrometry. *Environ. Sci. Technol.* **2015**, *49*, 13304.
(64) Wang, M.; Yao, L.; Zheng, J.; Wang, X.; Chen, J.; Yang, X.; Worsnop, D. R.; Donahue, N. M.; Wang, L. Reactions of Atmospheric Particulate Stabilized Criegee Intermediates Lead to High-Molecular-Weight Aerosol Components. *Environ. Sci. Technol.* **2016**, *50*, 5702−5710.
(65) Koizumi, H. Photoionization quantum yield for liquid squalane and squalene estimated from photoelectron emission yield. *Chem. Phys. Lett.* **1994**, *219* (1−2), 137−142.
(66) Beamson, G.; Briggs, D. *High Resolution XPS of Organic Polymers: The Scienta ESCA300 Database*; John Wiley & Sons, Inc.: Chichester, 1992.
(67) Zahardis, J.; LaFranchi, B. W.; Petrucci, G. A. Photoelectron resonance capture ionization-aerosol mass spectrometry of the ozonolysis products of oleic acid particles: Direct measure of higher molecular weight oxygenates. *J. Geophys. Res.* **2005**, *110* (8), 1−10.
(68) Vesna, O.; Sax, M.; Kalberer, M.; Gaschen, A.; Ammann, M. Product study of oleic acid ozonolysis as function of humidity. *Atmos. Environ.* **2009**, *43* (24), 3662−3669.
(69) Thiele, J. J.; Podda, M.; Packer, L. Tropospheric ozone: an emerging environmental stress to skin. *Biol. Chem.* **1997**, *378* (11), 1299−1305.


DOI: 10.1021/acs.jpca.6b09061
*J. Phys. Chem. A* XXXX, XXX, XXX−XXX